Volume 12
Number 23
7 December 2025
Pages 9855–10372

Materials Horizons

rsc.li/materials-horizons

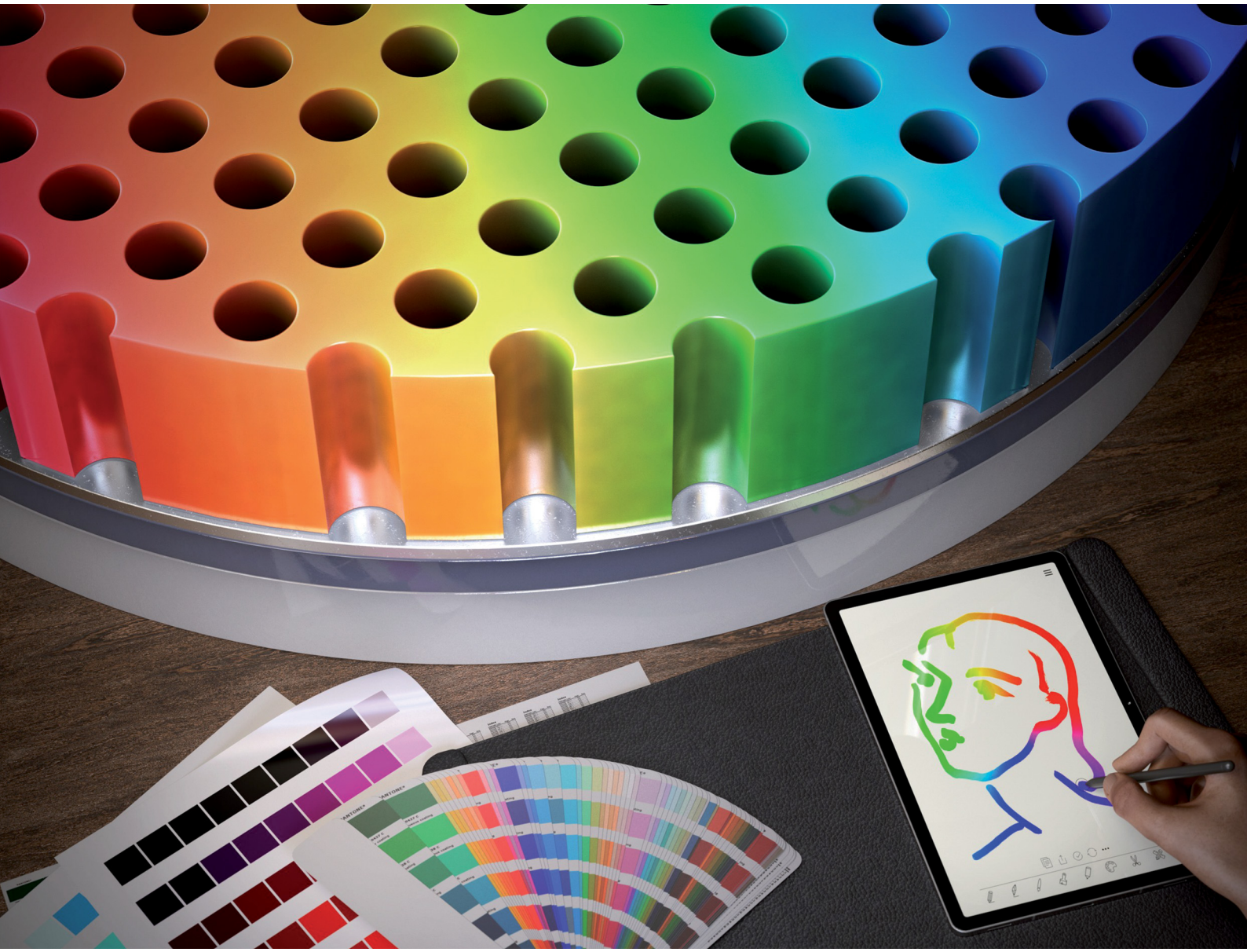

ISSN 2051-6347

ROYAL SOCIETY OF CHEMISTRY

COMMUNICATION

Soo-Hwan Jeong, Yun Seon Do *et al.*
Artwork-like multicolor structural coloration *via* spatially patterned anodic aluminum oxide with uniform-cavity design

Materials Horizons

ROYAL SOCIETY OF CHEMISTRY

COMMUNICATION

View Article Online
View Journal | View Issue

Check for updates

Cite this: *Mater. Horiz.*, 2025, **12**, 10059

Received 2nd September 2025,
Accepted 14th October 2025

DOI: 10.1039/d5mh01677k

rsc.li/materials-horizons

Artwork-like multicolor structural coloration *via* spatially patterned anodic aluminum oxide with uniform-cavity design

Hyo Jong Cho,[a] Jun Yong Kim,[a] Ki Won Jeong,[a] Soo-Hwan Jeong *[bc] and Yun Seon Do *[a]

Conventional dye-based color filters suffer from limited chemical stability and environmental durability. Structural color technologies that exploit nanophotonic phenomena offer a promising alternative; however, fabricating intricate nanostructures and multicolored patterns over a large area remains a significant challenge. Here, we present a scalable approach to artwork-like coloration by using spatially patterned anodic aluminum oxide (AAO) as the dielectric layer in metal–insulator–metal (MIM) cavities. Local modulation of the anodization conditions on a single aluminum film allows precise engineering of the effective refractive index values of the AAO layer. This introduces a conceptual shift: resonance is decoupled from geometrical factors and governed instead by porosity-driven refractive index modulation, a new design lever for nanophotonics. Consequently, diverse color domains are generated within a single cavity profile, enabling planar integration. Artwork-like multicolor patterns with aesthetic and functional impact are achieved on centimeter-scale substrates, and, because anodization is already an industrially established large-area process (used even in aircraft components), the method is inherently scalable to much larger surfaces.

New concepts

This work introduces a new paradigm for structural coloration by decoupling optical resonance from geometrical parameters and exploiting porosity-driven refractive index modulation in anodic aluminum oxide (AAO). Unlike conventional Fabry–Pérot or multilayered designs, which require distinct thicknesses and costly nanofabrication to achieve multiple colors, our approach demonstrates that diverse spectral responses can be encoded within a uniform-thickness cavity through localized modulation of nanoporous morphology.This advancement offers a scalable, lithography-free route to multicolor rendering, validated on centimeter-scale substrates. The uniform cavity AAO structures are achieved *via* complete anodization of an aluminum thin film, and local modulation of AAO porosity works as a versatile design method. The demonstrated artwork-like multicolor images highlight both the scientific precision and expressive versatility of the method. Because AAO anodization is already a widely used process for large aluminum components, the approach can be extended seamlessly to much larger surfaces. This compatibility underscores strong potential for industrial translation, where large-area, durable, and robust color platforms are required.The insight establishes index modulation as a general design lever in nanophotonics, shifting the field from geometry constraints to optics based on morphology and extending beyond coloration to metasurfaces, flat optics, anti-counterfeiting, and integrated optoelectronics.

Introduction

Color, brightness, saturation and resolution are fundamental parameters for handling visual information. In particular, color is the most precise and intuitive parameter, which is essential for object classification, visual perception, and aesthetic communication.[1] Color generation in nature is classified into two categories: material-based colors and structure-based colors. Coloring materials have intrinsic properties of selective absorption and reflection at specific wavelengths,[2] such as chlorophyll in plants[3] and hemoglobin in blood.[4] Structural colors are the outcome of optical phenomena such as interference,[5–7] diffraction[8–10] and resonance,[11–13] facilitated by submicron structures.[14–16] Without any coloration materials, selective spectral behaviors in nanostructured metasurfaces results in various chroma. These colors, which are observed in butterfly wings and bird feathers, exhibit vivid hues with extraordinary saturation and long-term stability.

In industrial fields including art, architecture, and fashion, color implementation has mainly relied on material-based technologies. Electronic devices also employ dye- and pigment-based color resists in color filter systems including displays and imaging sensors. However, its inherent dependence on material properties imposes several limitations. One major limitation is

[a] School of Electronic and Electrical Engineering, Kyungpook National University, Buk-gu, Daegu, 41566, Republic of Korea. E-mail: yuns.do@knu.ac.kr
[b] Department of Chemical Engineering, Kyungpook National University, Buk-gu, Daegu, 41566, Republic of Korea. E-mail: shjeong@knu.ac.kr
[c] School of Chemical Engineering and Applied Chemistry, Kyungpook National University, Buk-gu, Daegu, 41566, Republic of Korea

its poor environmental stability, as it remains susceptible to ultraviolet radiation, thermal stress, and chemical degradation.[17] The size of pigment particles is an additional obstacle for obtaining high quality of color. Submicron particles increase scattering and consequently reduce saturation, whereas conventional larger pigments ($\sim$10 μm) decrease pixel density and resolution.[18]

In contrast, structure-based colors provide material-independent, high-resolution color control *via* light–matter interaction on subwavelength scales, with remarkable stability and reproducibility. Although nanophotonic phenomena such as surface plasmons, Fabry–Perot (FP) interference and photonic bandgaps, are well organized in classical theory, their practical implementation remains a significant challenge. The fabrication technology of nanostructures has seen remarkable advancements since the early 2000s, expanding their applicable domains. Nevertheless, most of the structural colors encounter constraints regarding scalability and manufacturing cost. Generally employed nanopatterning methods such as electron-beam lithography or focused ion beam processing are costly and time-consuming[11,12] for mass production. For these reasons, most reported studies have demonstrated various hues and intricate patterns in the microscale ($\sim \mu m^2$), or are often limited to single-chroma reproduction when scaled up to the centimeter-scale.[19–21]

In this study, we suggest a novel approach to structural coloration by incorporating a spatially modulated anodic aluminum oxide (AAO)[22] layer as the insulator in a metal–insulator–metal (MIM) structure. The MIM structure shows superior color selectivity based on FP interferences, and consists of stacks of thin films, quite simple compared to other structural colors. Since the resonance wavelength is dependent on the cavity thickness,[23,24] different thicknesses are required for RGB implementation, and multilayer fabrication and additional masking steps are required.[25,26] Unlike thickness-dependent FP tuning, our method leverages porosity-driven refractive index engineering to achieve color selectivity in a constant-thickness cavity, establishing a new methodology in structural coloration. This enables multiple resonance wavelengths to be achieved within a constant thickness MIM cavity, addressing the conventional limitation of thickness-dependent tuning. Importantly, lithography-based multicolor implementation usually demands multiple masks,[25,26] overlay-critical steps,[27] photoresist coat/bake/develop cycles,[28] and dry/wet etching,[29] particularly when RGB is achieved by thickness-split cavities.[23,24] By contrast, our approach achieves nanoscale patterning through self-organized AAO in a single, low-temperature wet step without the need for a photoresist or etching. Spatial selectivity is introduced lithography-free by selective anodization (using simple local masking during anodization) and a single shadow-mask deposition for artwork patterns. Combined with the constant-thickness cavity design, these factors reduce process complexity and reliance on capital lithography tools, providing a cost-effective route that is compatible with established industrial anodization.[22,30–33] By employing anodization, a simple and industrially common process, we generate vivid multicolor patterns without lithography. The proposed fabrication flow with a thin-film type of aluminum (Al) and spatial growth of AAO could realize the artwork-like and scalable multicolor patterns in a single substrate. As anodization is already being practiced on large Al surfaces (even aircraft wings),[30,33] our strategy can be seamlessly scaled from centimeter demonstrations to wafer- or industrial-scale devices.

Experimental section

Device design and analysis

The resonant wavelengths and effective refractive index were calculated using MATLAB (MathWorks, USA). Based on the calculated optical parameters, the device transmittance was analyzed using finite-difference time-domain (FDTD) simulations (Lumerical FDTD Solutions, Ansys Inc., Canada). The electric field distribution was also calculated to investigate the optical resonance properties within the device. The simulation was performed in 3D with the antisymmetric boundary conditions along the *x*-axis and the symmetric boundary conditions along the *y*-axis, which simultaneously minimize computational costs while effectively representing an infinitely periodic structure in *x*–*y* lateral directions. A perfectly matched layer (PML) was applied along the *z*-axis to suppress spurious reflections and mimic open boundaries. This boundary condition setup corresponds to an infinitely repeated unit-cell array in the *x*–*y* plane, consistent with the quasi-periodic ordering of the fabricated AAO films. The maximum mesh step size was set to 1 nm to ensure numerical precision near the active region. A plane wave source with a wavelength range of 380–780 nm was incident along the +*z* direction. The transmittance monitor was placed 1 μm above the structure, while the electric field monitor was configured to capture the cross-sectional field distribution within the device.

Device materials

Tungsten oxide (WO_3), silver (Ag), and Al were purchased from iTASCO in South Korea and were used as an adhesion layer (capping layer) and a reflector and a precursor for AAO.

Preparation of thin aluminum film specimens

Glass substrates were ultrasonically cleaned in acetone and isopropyl alcohol (IPA) for 15 minutes each, followed by air drying. For flexible configurations, polyethylene terephthalate (PET) films were laminated onto the pre-cleaned glass substrates. To enhance film adhesion, all substrates underwent ultraviolet-ozone treatment for 20 minutes. Subsequent sequential thermal evaporation of WO_3 (70 nm), Ag (20 nm), and Al (250 nm) was performed under a nitrogen atmosphere at a base pressure below 5×10^{-6} Torr. The deposition rates were as follows: WO_3 and Ag at 1 Å s^{-1}, and Al at 2 Å s^{-1}.

Formation of the AAO layer

To define spatially selective anodization areas, the Al-coated specimens were partially masked using commercial nail polish. The electrolyte solution was prepared by mixing 1.0 M citric acid and 0.15 M oxalic acid (total volume: 300 mL) with continuous magnetic stirring. Anodization was conducted in a jacketed beaker setup with a recirculating coolant bath to

maintain the electrolyte at 3 °C. The copper (Cu) electrode and Al-coated substrate served as the cathode and anode, respectively, and had a distance of 5 cm from each other. A DC voltage of either 55 V (red) or 107 V (green and blue) was applied to initiate anodization. After complete anodization of the Al film, the specimens were rinsed sequentially in acetone and IPA. Pore widening was performed by immersing the samples in 5 wt% phosphoric acid at 40 °C for a controlled duration (Red: 20 min, Green: 0 min, Blue: 40 min, Gradual color: 0–40 min). The masking and anodization process was repeated N times to define multiple regions, each associated with distinct anodization conditions.

Fabrication of MIM structures with patterning

Following the anodization process, the samples were further deposited by sequential thermal evaporation of Ag (20 nm) and WO_3 (70 nm) onto the porous AAO layer. To create artistic patterns such as Henri Matisse-inspired motifs or university logos, a shadow mask was applied during deposition. The deposition rates were as follows: WO_3 and Ag at 1 Å s^{-1}.

Device characterization

The optical transmittance of the fabricated single-color (monochromatic) devices was measured using a UV-visible spectrophotometer (LAMBDA 365; PerkinElmer, MA, USA). The structural and morphological properties of the thin films were analyzed using a field emission scanning electron microscope (FE-SEM, SU8230; Hitachi, Japan). To visually evaluate the chromatic performance of the device, photographic images were captured by placing the sample atop a diffuser film illuminated with an incandescent light source. Device images were taken using a high-resolution smartphone camera (iPhone 15 Pro, Apple Inc.) by placing the sample on a diffuser-covered incandescent lamp to visualize transmitted color.

Results and discussion

Optical design of the uniform-cavity meta-MIM

Fig. 1a and b depict a schematic of the proposed meta-MIM structure, designed to facilitate selective optical resonance wavelengths while maintaining a uniform physical cavity thickness. For generating the FP interference, the device structure consisted of a 250 nm-thick cavity layer sandwiched between two 20 nm-thick Ag reflectors, a thickness chosen as it provides effective reflectivity while minimizing optical losses (see Fig. S1). A bottom WO_3 layer is deposited under the bottom Ag reflector to improve adhesion to the substrate, while top WO_3 capping layer on the top Ag facilitates efficient light extraction as shown in Fig. S2. As the thickness of the outer capping dielectric layer increases, the transmittance properties of the meta-MIM structure are enhanced. As shown in Fig. S2, when the capping layer thickness reaches 70 nm, the RGB device exhibits the highest resonance peak intensity with minimized wavelength shifts. At this optimal thickness, the full width at half maximum (FWHM) is also reduced, indicating improved color purity. The outer capping layer has a negligible influence on the phase difference between the reflective and cavity layers. It significantly enhances impedance matching at the cavity/air interface, thereby facilitating more efficient light extraction. Consequently, reflection losses are suppressed, and the precision of the FP cavity is improved, leading to an amplified resonance peak transmittance without perturbing the intrinsic resonance conditions.

The dimensions of the anodic alumina layer, including interpore distance and pore diameter, are considerably smaller than the operating wavelengths in the visible regime. Under such subwavelength conditions, the AAO cannot be treated by simple ray optics; instead, the porous structure can be regarded as an effective homogeneous medium from the electromagnetic perspective. In this approach, light propagation is described by an averaged refractive index that depends on the porosity of the layer. Eqn (1) therefore represents the effective refractive index (n_{eff}) of the porous AAO, calculated by applying an effective medium approximation that accounts for the volume fractions of alumina and air. As the porosity increases, n_{eff} decreases toward the refractive index of air, while lower porosity results in a higher n_{eff} closer to bulk alumina. This effective index treatment provides a valid approximation for modeling the optical response of the AAO cavity and is commonly employed in porous photonic films. This optical design method relies on modulating the n_{eff} of the AAO layer to achieve various resonance wavelengths. The values of n_{eff} refer to the volume-averaged refractive index of the nanoporous Al_2O_3 cavity layer, which is tunable through control of the pore geometry. The n_{eff} is calculated based on the porosity (φ) of a hexagonally arranged pore structure as follows,

$$n_{\mathrm{eff}} = \sqrt{\varphi \times {n_{\mathrm{air}}}^2 + (1-\varphi) \times {n_{\mathrm{Al_2O_3}}}^2}, \quad \left(\varphi = \frac{\pi \times {D_{\mathrm{p}}}^2}{2\sqrt{3} \times {D_{\mathrm{int}}}^2}\right) \tag{1}$$

where n_{air} is the refractive index of air, $n_{\mathrm{Al_2O_3}}$ is the refractive index of alumina, D_{p} denotes the diameter of pores, and D_{int} is the distance between adjacent pores. Given the low optical dispersion of Al_2O_3, its refractive index values hardly change across the visible range. The achievable range of n_{eff} ranges from 1.1 to 1.8, as shown in Fig. 1c. This demonstrates that precise optical tuning is possible by controlling the interpore distance (D_{int}) and pore diameter (D_{p}) during fabrication.

The cavity consists of an AAO layer with a nanoporous, where n_{eff} is tunable by porosity control as follows,

$$-\Delta\varphi_{\mathrm{top}} - \Delta\varphi_{\mathrm{bottom}} + 2n_{\mathrm{eff}}\mathrm{d}k_0 = 2m\pi, \quad \left(k_0 = \frac{2\pi}{\lambda_0},\ m = 0, 1, 2, 3\ldots\right) \tag{2}$$

where $\Delta\varphi_{\mathrm{top}}$ is the reflection phase of the top Ag layer (Top_Ag), $\Delta\varphi_{\mathrm{bottom}}$ is the reflection phase of the bottom Ag layer (Bottom_Ag), and d is the thickness of the AAO cavity. Within the MIM, multiple internal reflections occur between the top and bottom Ag reflectors. Constructive interference is achieved

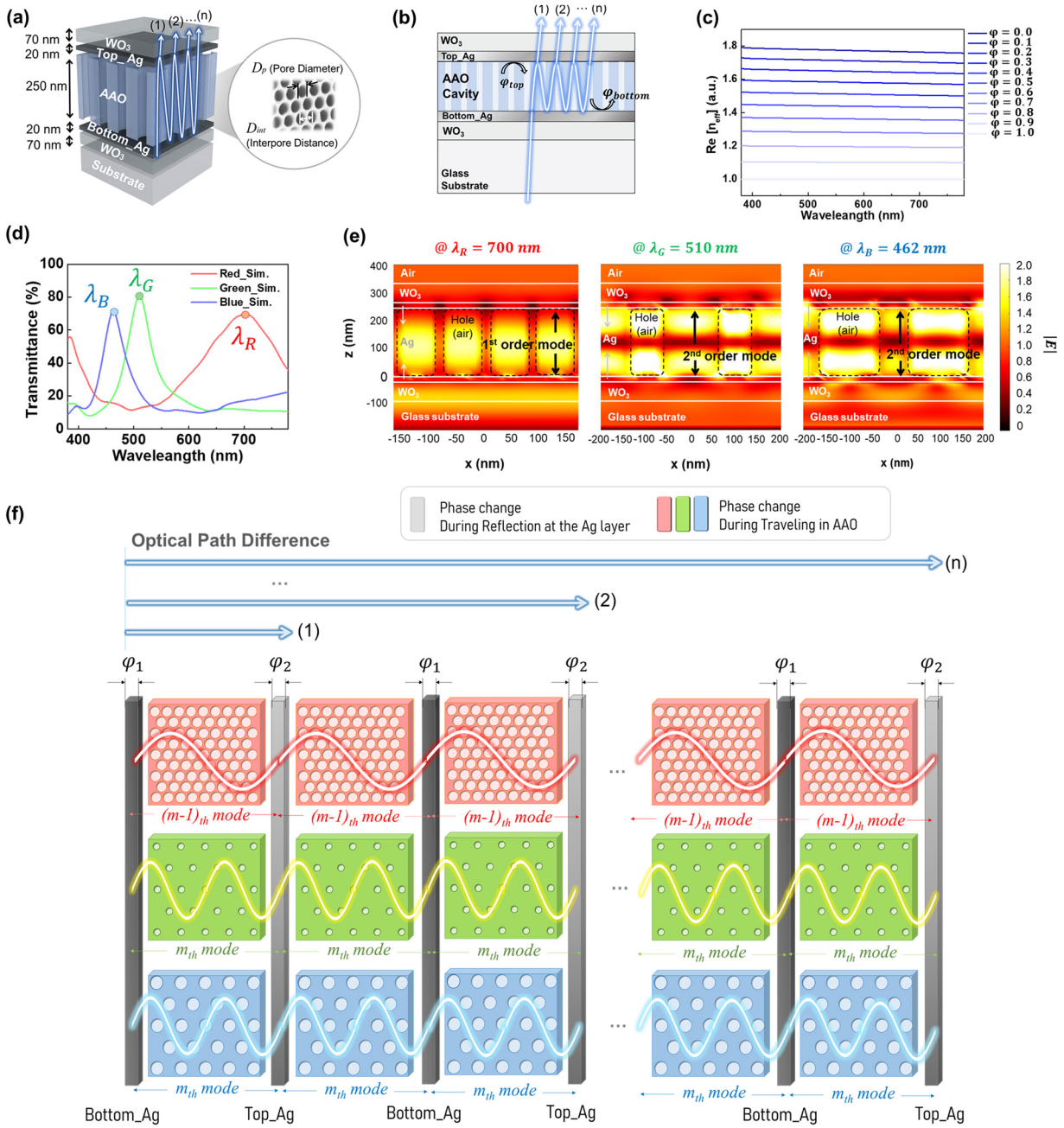

Fig. 1 (a) Schematic of optical designed meta-MIM. (b) Schematic of light propagation through designed meta-MIM. Incident light undergoes multiple internal reflections between the top and bottom Ag layers, with phase shifts occurring at each interface and within the porous AAO cavity, enabling resonance-based structural colortion. (c) The real part of the effective reactive index according to the porosity. (d) Simulated transmittance spetra of meta-MIM with n_{eff} values designed to obtain the RGB primary colors. (e) The electric field profile at the resonance wavelength for each RGB structure. The number of antinodes confirms that red is in first order mode and green and blue are in second order mode. (f) Resonance behaviors of RGB colors in a nanoporous AAO cavity with Ag reflectors.

when the total phase shift satisfies the multiples of 2π, resulting in narrowband resonance at a specific wavelength.

The resonant wavelength is determined by the cavity thickness, reflection-induced phase shifts, and the travelling phase of light in the cavity, which is determined by n_{eff}. As shown in Fig. 1d, the resonance wavelengths of the primary colors, the red (R), green (G), and blue (B), are modulated through the control of n_{eff} under a constant cavity thickness condition. Fig. 1d shows that the simulated transmittance spectra of the RGB meta-MIM structures exhibit resonance peaks at the designed wavelengths of 700 nm (R), 510 nm (G), and 462 nm (B). These resonant modes are caused by constructive interference within the cavity layer of constant thickness and demonstrate high spectral selectivity. The intensity of each peak indicates the efficiency of light transmission through the nanoporous cavity under resonant conditions. Resonance wavelengths of 700 nm, 510 nm,

and 462 nm are achieved within the 250 nm cavity, corresponding to n_{eff} = 1.26 (R), 1.73 (G), and 1.56 (B), respectively, with porosity (φ) of 0.70 (R), 0.08 (G), and 0.32 (B).

For the red chroma, the constructive interference mode corresponds to the first-order resonance mode, whereas the green and blue chroma originate from the second-order resonance mode. Simulated electric field profiles for the RGB structures are shown in Fig. 1e. The red device exhibits four periodic units, while the green and blue devices show two periodic units each. The black dashed lines indicate the positions of the AAO holes. The red device exhibits a single antinode, which is indicative of a fundamental (first-order) mode, while two antinodes are observed in the green and blue structures, corresponding to second-order resonance modes. These field profiles are in excellent agreement with the design model presented in eqn (2). As illustrated in Fig. 1f, the Ag–AAO cavity interface introduces wavelength-dependent reflection phases, and the corresponding calculated phase spectra are provided in Fig. S3. The combined reflection phases of Ag–AAO ($\Delta\varphi_{top} + \Delta\varphi_{bottom}$) and propagation phase ($2n_{eff}dk_0$) within the AAO cavity satisfy a total phase of $2m\pi$ (R: m = 0, G and B: m = 1), depending on the effective optical path determined by the porosity and thickness. In this structure, the red corresponds to a first order mode, whereas the green and blue represent second order mode. The total phase difference, including both propagation and reflection components, satisfies the resonance condition of $2m\pi$ for each color. This enables spectrally selective resonance within the same physical cavity thickness (250 nm), by tuning the n_{eff} *via* porosity modulation.

Fig. 2a depicts the transmission spectra at various porosities. The red line corresponds to a first-order resonance mode, while the other colors represent a second-order resonance mode. As the porosity increases, the resonance wavelength shifts toward the blue. The estimated n_{eff} values align well with the theoretical values derived from eqn (2).

The color palette was calculated from a parametric sweep of the nanoporous cavity design, in which the interpore distance (D_{int}: 50–400 nm) and pore diameter (D_p: 20–400 nm) are varied independently, as shown in Fig. 2b. This two-dimensional design space allows continuous modulation of n_{eff} of the AAO cavity. This allows wide range tunability for the resulting structural colors while maintaining the physical cavity thickness unchanged. The light brown area in the palette represents the physically unattained configurations where D_p exceeds D_{int}, indicating a pore-dominant regime with n_{eff} approaching to that of air.

Fig. 2c shows the simulated spectral outputs of the cavity structures in the CIE 1931 color coordinate system, providing an intuitive visualization of the achievable color gamut. Each plotted point corresponds to a distinct (D_{int}, D_p) combination and demonstrates that a single-cavity configuration can support a wide range of vivid, high-purity colors. This highlights the ability of the proposed design to deliver full-color images through precise control of nanostructural parameters.

For the selective control of a single resonant wavelength within a cavity on the subwavelength-scale, the use of low-order resonant modes is essential. As a result, the cavity length must be confined to less than 300 nm, which confines the design range for photonic structure. The effective refractive index is tunable in the range of 1.1 to 1.8. In our structure, the blue–green resonances originate from the second-order mode, which is relatively insensitive to reflection-phase variations at the Ag/AAO interfaces. By contrast, the yellow–red region corresponds to the first-order resonance, which is more strongly influenced by the wavelength-dependent reflection phases of Ag. When eqn (2) is applied to the yellow spectral region ($\approx$580 nm), the propagation phase must contribute $\sim$1.6π (for m = 0) or $\sim$3.6π (for m = 1) in order to satisfy the total phase condition. This corresponds to n_{eff} of approximately 0.92 or 2.1. Such values lie well outside the physically attainable range of porous AAO (1.1–1.8), thereby preventing the formation of a resonance in this region. This quantitative analysis clarifies why the yellow channel does not emerge in the actual spectra, whereas the RGB resonances remain accessible within the achievable design space. Despite these limitations, it is still possible to achieve distinct resonances at the primary RGB wavelengths. This is

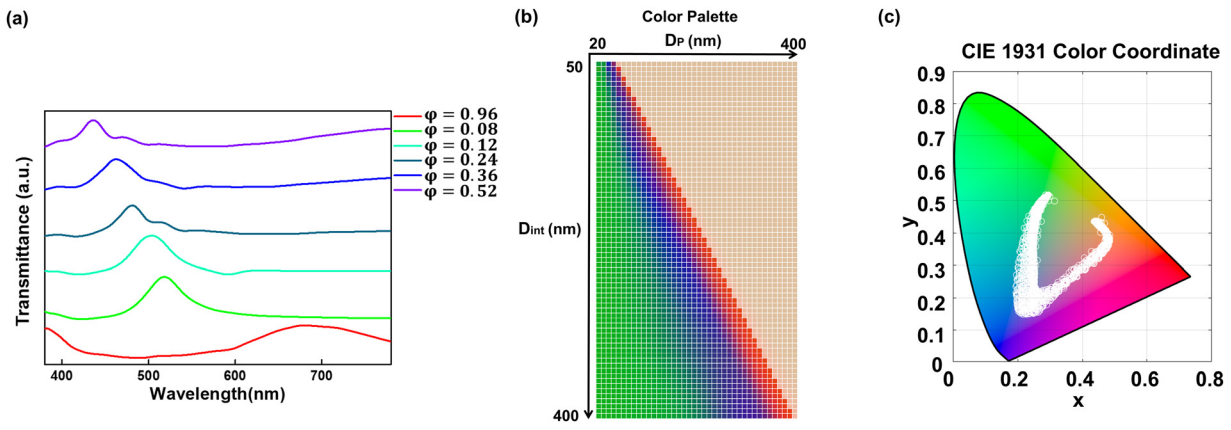

Fig. 2 The optical properties of designed meta-MIM. (a) Transmittance spectra at various porosities. The red chroma has first order resonance mode, and the rest of the colors have the second order resonance mode. (b) The color palette is shown for the transmittance obtained according to D_{int} and D_p. The light brown color palettes are physically unattainable dimensions when D_p is greater than D_{int}. (c) The transmittance obtained according to D_{int} and D_p is CIE 1931 color coordinate.

particularly significant for color-selective imaging applications, where the excitation of red, green, and blue resonances is the foundational requirement for color reproduction.

Fabrication flow of the meta-MIM by using a spatially modulated AAO process

The fabrication process of the meta-MIM structure incorporating an AAO for refractive index modulation within the cavity is illustrated in Fig. 3. The process deposits the sequential thermal evaporation of WO_3 (70 nm), Ag (20 nm), and Al (250 nm) onto a flexible (polyethylene terephthalate) or rigid (glass) substrate. The thickness of the Al layer is precisely matched to the desired cavity thickness (250 nm) which is converted to a nanoporous oxide layer by anodization. In addition to the oxalic-acid-based bath used here (1.0 M citric acid + 0.15 M oxalic acid at 3 °C), porous AAO can also be formed in sulfuric and phosphoric acids. In AAO, the D_{int} scales approximately linearly with anodization voltage ($\sim$2.5 nm V^{-1}), and widely used self-ordering windows are $\sim$25 V (H_2SO_4), $\sim$40 V ($H_2C_2O_4$), and $\sim$195 V (H_3PO_4).[31,34,35] Accordingly, relative to oxalic acid, sulfuric acid typically yields smaller D_{int} and D_p with higher pore number density, while phosphoric acid yields larger D_{int} and D_p with lower pore number density. In our uniform-thickness MIM cavity, the electrolyte thus shifts the accessible (D_{int}, D_p) space and the resulting φ and n_{eff}. A decrease in φ (higher n_{eff}) tends to red-shift the resonance at a given order m, whereas an increase in φ (lower n_{eff}) tends to blue-shift it; however, the precise spectral position also depends on resonance order and interface phase contributions. These trends do not alter the operating principle; they inform process window and palette design. High-field phosphoric-acid anodization ($\sim$195 V) is feasible but requires careful thermal management to avoid local burning.[34–36] In this work, a mixed oxalic–citric electrolyte was adopted to combine the stable ordering capability of oxalic acid with the broader anodization window of citric acid.[37,38] The recipe was optimized by preliminary experiments, and concentrations can be tuned depending on the intended color palette.

To enable n_{eff} tuning, nanoporous patterning is introduced using a self-ordered AAO process. Prior to anodization, nail polish masking is applied to separate the working areas as a drawing-like approach, allowing the formation of several different nanostructures on a single substrate. Anodization is then obtained by applying a controlled voltage in an acidic electrolyte, forming a vertically aligned Al_2O_3 nanopore array with specific dimensions of D_{int} and D_p. The dimension of D_{int} is directly proportional to the applied voltage, while that of D_p can be independently adjusted through a pore-widening process.[31] In regions coated with nail polish, the electric field is excluded and anodization does not occur, enabling spatial pattern variation. After anodization, the specimen is rinsed with acetone and IPA. To create multiple colors ('N' configurations) on the same substrate, the above steps are repeated N times with different pore-widening durations, allowing selective modulation of D_p under fixed D_{int} conditions.

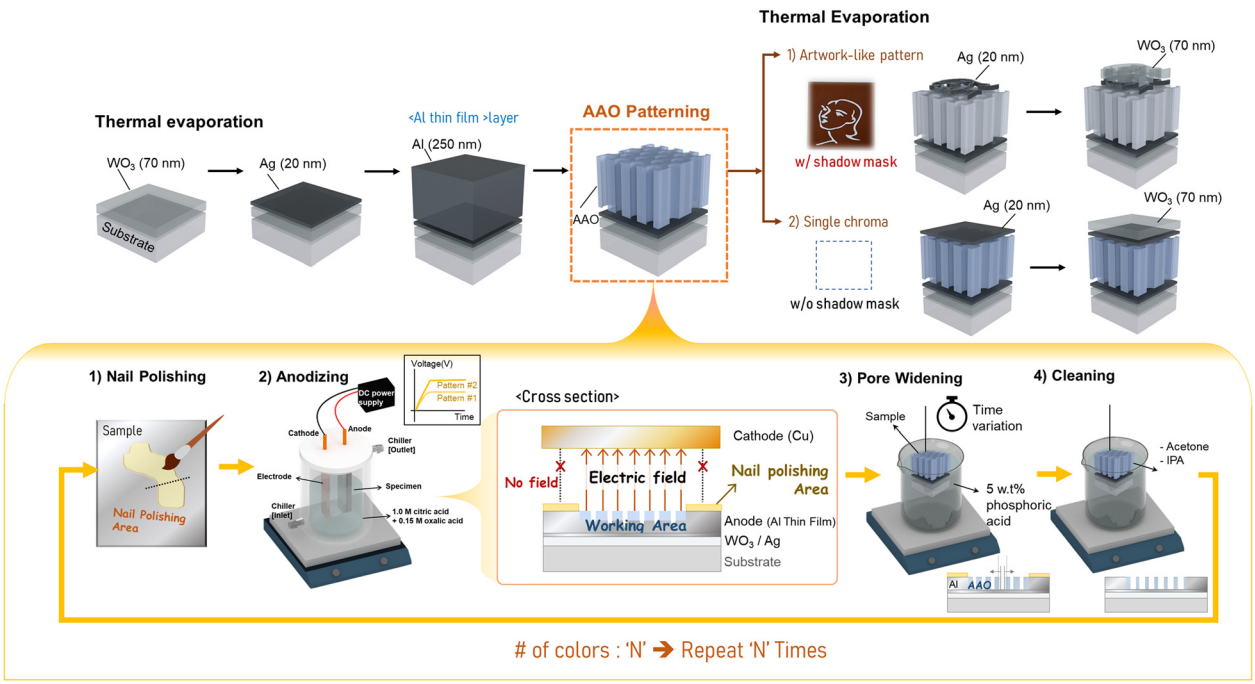

Fig. 3 Fabrication process of the meta-MIM using the AAO process. Process flow for the fabrication of the meta-MIM. Thermal deposition for thin film formation and AAO process for nanopatterning are performed. First, WO_3, Ag, and Al are sequentially deposited onto the substrate using thermal evaporation. Nail polishing is performed for spatially modulated anodizing to obtain various patterns within a single substrate. The thin film Al in each working area undergoes sequential anodization. Pore widening is performed under the appropriate conditions to control the pore size. Finally, for the formation of the MIM structure, Ag and WO_3 are sequentially deposited. During the artwork creation, the deposition of Ag/WO_3 is performed using a shadow mask to define the structure.

In addition, to achieve gradual coloration, spatial modulation of the pore diameter was realized by controlling the pore widening duration in a region-dependent manner. Without a repeated masking process, this can be accomplished by progressively immersing different regions of the sample in phosphoric acid, thereby inducing spatial variation in the etching time. After pore engineering, the MIM structure is completed *via* the deposition of a top Ag reflector (20 nm) and a WO_3 capping layer (70 nm) to improve the optical outcoupling as illustrated in Fig. S2a. At this stage, shadow mask is used for artwork or specific patterning.

Fig. 4 illustrates the experimental results of the fabricated meta-MIM structures, including measured transmittance spectra, photographs, and field emission scanning electron microscope (FE-SEM) images of the uniform-cavity meta-MIMs. The single chroma of R, G, and B were fabricated in a 2 cm × 2 cm area. As shown in Fig. 4b, the transmittance spectra and corresponding photographic images of the R, G, and B structures reveal resonance wavelengths at 700 nm (R), 521 nm (G), and 441 nm (B). The peak positions of the green and blue devices have shifted slightly compared to the designed values. The peak intensities were measured to be 46.6% (R), 31.04% (G), and 33.33% (B), representing a 30–50% reduction compared to the simulation results.

This deviation originates from two main sources. Firstly, the optical simulations were based on well-ordered AAO nanostructures. The systematic regular patterns, typically achieved through a two-step anodization process[31] require thick Al media. In contrast, the suggested devices were fabricated using a single-step anodization with a thin Al film, leading to lower pore ordering and irregular morphology, as shown in Fig. 4c and d. Moreover, incomplete pore penetration was observed in some regions, introducing additional structural irregularities. This structural disorder reduces the quality of optical resonance.

Second, surface roughness and thickness variations at the top surface of the porous AAO layer can lead to non-uniform deposition of the top Ag and WO_3 layers. These irregularities distort the FP resonance condition by disrupting phase matching within the cavity. In particular, since the resonant phase shift is highly sensitive to the reflective phase of Ag, even minor roughness can induce phase errors, resulting in spectral shifts and transmittance loss. Overall, the measured red-shift and reduced transmittance are attributed to these optical non-idealities of the fabricated structures. Nevertheless, these results validate the proposed design approach and suggest that precise color reproduction can be further improved through process optimization and thin-film quality control.

As shown in Fig. S4, the FDTD optical simulation results based on SEM-derived structures exhibit better agreement with the experimental data than those based on idealized geometries. This improved correspondence arises from the incorporation of actual morphological features observed in SEM images, such as irregular pore shapes and incomplete hole penetration. To more accurately reflect the real morphology seen in Fig. 4e—where certain nanopores do not fully penetrate through to the bottom Ag layer—a modified FDTD model was constructed by introducing randomly distributed non-penetrating holes with residual thicknesses of approximately 30–50 nm. This modification enabled a more realistic optical response by accounting for the imperfect pore formation commonly found in the fabricated AAO.

In particular, for the blue device, the simulated resonance wavelength appears at 454 nm, while the experimental value is 432 nm—showing a blue shift of approximately 22 nm, yet preserving the overall spectral shape. The SEM-based simulated peak transmittance was 43.73%, while the experimental value was 33.36%, corresponding to a reduction of 23.7% relative to the simulation results. This discrepancy is primarily attributed

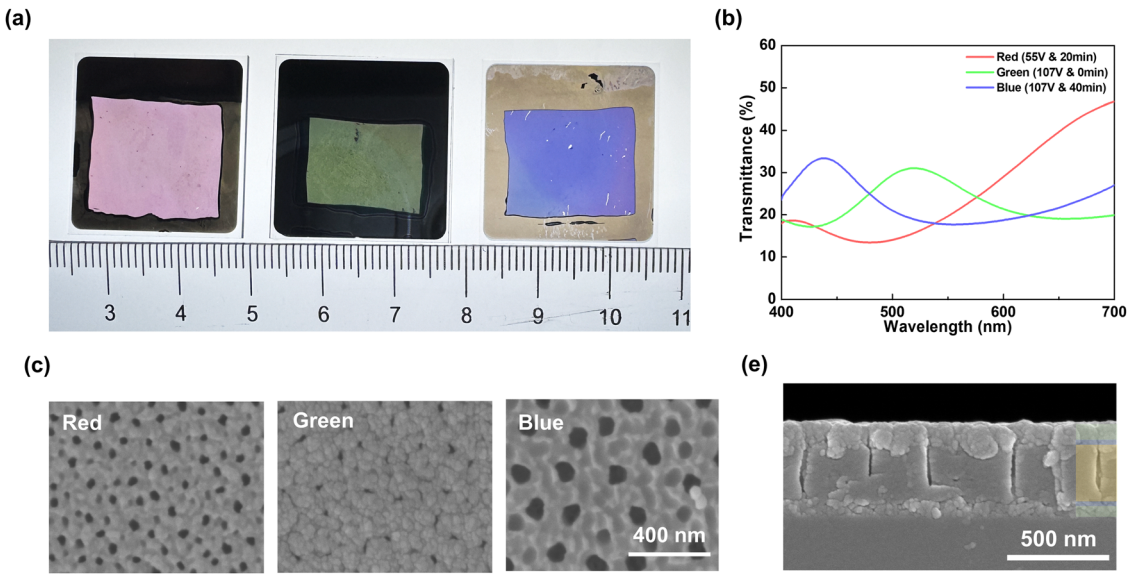

Fig. 4 The measured transmittance spectrum and photo image of fabricated meta-MIM using AAO process. (a) The photo image of fabricated meta-MIM in RGB colors. (b) The measured transmittance spectrum of (a). (c) and (d) SEM image of the (a) structure. (c) Top-view for each rgb filter without upper Ag/WO_3 layer. (d) Cross-section view is a green filter.

to imperfect surface flatness of the AAO layer and the deposited films, which introduce deviations from ideal FP cavity conditions. This interpretation is further supported by atomic force microscopy (AFM) images in Fig. S5, which reveal that the AAO-based structure exhibits significantly higher surface roughness than the reference device, with root mean square (RMS) roughness values of 8.557 nm and 2.516 nm, respectively. Additionally, the broader FWHM observed in the experimental spectrum is attributed to thickness non-uniformity and morphological imperfections in the AAO structure, both of which degrade spectral confinement within the resonance cavity.

A critical aspect of the proposed fabrication procedure is that the Al medium utilized to create the AAO layer must be deposited as a continuous single film throughout the entire substrate. This approach provides sufficient electrical continuity, helping to maintain a stable electric field during anodization, as explained in Fig. S6. If an artwork-like or free-styled pattern is pre-defined during Al deposition prior to anodization, the zero potential areas due to the electrical discontinuity are not available for oxidation. Because of the thin film thickness, the Al media undergo fully processed oxidation and convert to insulating media, thus stopping the electric channel. Thin film Al and fully anodization realize a uniform thickness of the cavity. Furthermore, since conductor surfaces are fundamentally equipotential, the direction and strength of the local electric field might become skewed near the borders of patterned patches, inducing lateral growths of the pores.

Fabricated artwork-like meta-MIM

Based on the spatially modulated AAO fabrication technique outlined above, we implemented various multicolor meta-MIM structures on a single substrate. This section highlights the practical realization of artwork-like coloration using the proposed method, including a detailed examination of its optical performance and scalability. Fig. 5 illustrates the achievement of full-color and multi-color artworks on a single substrate, fabricated without employing any complex lithography techniques. This result confirms that multiple optical colors under a constant cavity thickness, exclusively by structural modulation of the nanoporous AAO layer. Compared to previous approaches that achieved multicolor representation at the micrometer scale, or single-color patterns over centimeter-scale areas, this study achieves multicolor rendering on a single centimeter-scale substrate, representing a significant advance in spatial and chromatic scalability.

Fig. 5 illustrates the versatility of AAO-based structural coloration through a series of spatially patterned demonstrations. Within a single substrate, we reproduced a replica of *Nadia aux cheveux lisses* by Henri Matisse with gradual-color and campus nameplates (KNU) with multi-color, emphasizing the convergence of scientific precision and artistic expression. In Fig. 5a, the letters ''K'', ''N'', and ''U'' are displayed in different colors on a single substrate. These colors were realized by spatially varying the AAO pattern in each region within a uniform cavity. Fig. 5b confirms that the same fabrication strategy can be applied to flexible substrates, maintaining both color integrity and mechanical stability during bending. Fig. 5c presents the original line drawing *Nadia aux cheveux lisses* by Henri Matisse, which served as the design motif. The corresponding shadow mask, shown in Fig. 5d, was used to reproduce the artwork using a single-step deposition process. This avoided complex lithographic alignment and enabled high-fidelity patterning over a large area.

Finally, Fig. 5e demonstrates gradual color variation within a single image, achieved by continuously tuning the AAO pore diameter. This result illustrates the ability of the method to spatially pattern both discrete and continuous color information, opening possibilities for scalable fabrication of multifunctional and visually expressive nanophotonic elements.

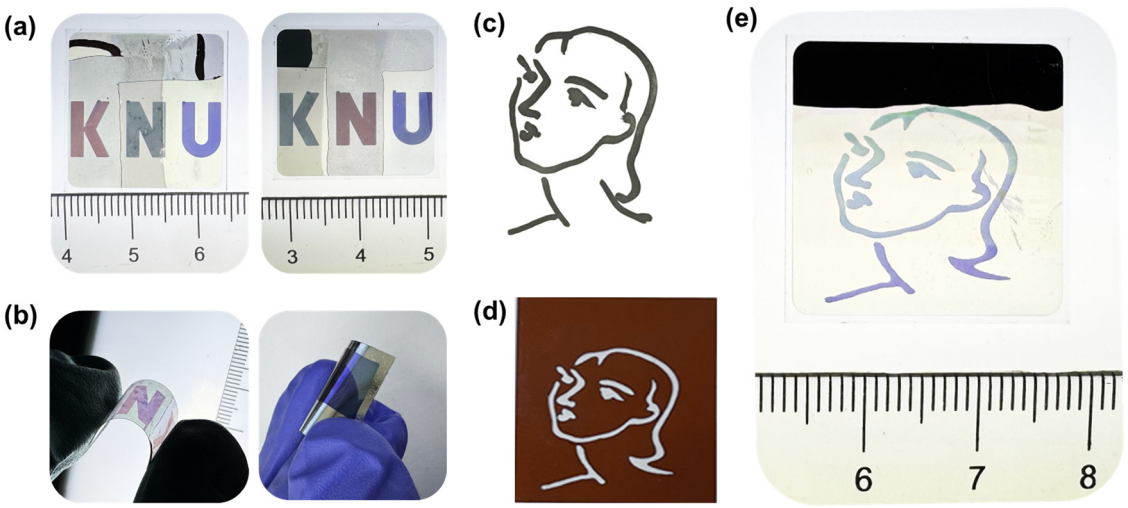

Fig. 5 Photo image of fabricated meta-MIM. (a) University nameplate (KNU) on single substrate, primary color (R/G/B, and G/R/B) using a meta-MIM. (b) University nameplate and single-color on flexible substrate. (c) Photo image of Henri Matisse's orignial artwork 'Naida aux cheveux lisses'. (d) Shadow mask of (c) artwork, enabling selective deposition for the Top_Ag and WO_3 layers. (e) Gradual color of Henri Matisse's 'Naida aux cheveux lisses' reproduced on a single substrate *via* spatially controlled meta-MIM.

Notably, the entire image was patterned using a single shadow mask, and color separation was accomplished through selective deposition of the top reflective layer. This eliminates the need for complex mask alignments or multiple masking steps, thereby simplifying the fabrication.

The proposed meta-MIM modulates n_{eff} within the AAO cavity of constant thickness, enabling precise optical resonance tuning. This is obtained through the geometric control of a nanoporous AAO layer, where the D_{int} and D_p determine the n_{eff}. The resonance conditions defined in Eqn (2) enable resonance wavelength control on large-area substrates, relying primarily on this geometric modulation rather than on cavity thickness or material. The proposed optical design maintains the benefits of FP, as it can be adjusted by the average porosity ratio rather than accurate periodicity or size control in the AAO pattern. Simulations confirmed RGB resonances could be tuned by n_{eff} at constant cavity thickness. Fabricated devices exhibited visible colors but with slight spectral shifts and lowered intensity due to roughness and pore irregularities. This validates the conceptual advance of decoupling resonance from geometry to porosity-driven index control.

Specifically, surface roughness and pore irregularities in the single-step anodized AAO layer hinder uniform deposition of the upper Ag and WO_3 layers. These imperfections introduce phase mismatches in the cavity, resulting in spectral deviations and broadened transmittance profiles. To address these issues, future work could explore the use of ultrathin buffer layers such as atomic layer deposition (ALD) to improve the planarity of the AAO surface without compromising porosity. Additionally, employing oblique-angle metal evaporation or implementing mild post-anodization surface etching may help achieve smoother top interfaces, thereby enhancing FP resonance fidelity. These refinements can further improve color purity and transmittance efficiency, expanding the practical applicability of meta-MIM systems.

Nevertheless, the close alignment between measured and simulated spectra confirms the robustness of the design strategy. In addition, the meta-MIM exhibits remarkable scalability and spatial multiplexing capabilities. For large area applications, recent advances in printing-based structural coloration including nanoimprint lithography (NIL), inkjet printing, and roll-to-roll (R2R) processes, have enabled centimeter-scale multicolor rendering with high throughput.[39–45] But these approaches typically rely on costly mold fabrication, residual layer removal, and overlay critical alignment. Inkjet printing provides mask-free, digital patterning with design flexibility, yet its resolution remains limited to the micrometer scale and uniformity is challenged by droplet variability. In contrast, our AAO-based approach realizes color selectivity in a constant-thickness FP cavity through porosity-driven effective refractive index modulation, thereby eliminating thickness splitting and high-resolution lithography. Because the nanoporous AAO is formed by self-ordering in a single low temperature wet step, spatial selectivity can be realized *via* selective anodization and a single shadow mask deposition. This combination offers process simplicity, compatibility with photolithography for more complex designs, and industrial scalability, as anodization is already practiced over meter-scale aluminum components. While the optical figure-of-merit (intensity/FWHM) of our devices remains comparable to previously reported dielectric[46–48] or plasmonic filters,[49–51] the unique advantage of our method lies in its scalability and versatility, enabling multifunctional full color designs such as artwork reproduction and flexible integration. This constitutes a distinct performance axis beyond spectral purity alone.

Localized masking and selective pore expansion can be used to pattern distinct nanoporous geometries on a single substrate, supporting spatially resolved multicolor rendering at uniform cavity thickness. The artwork-like nature of these demonstrations emphasizes expressive versatility, suggesting applications in anti-counterfeiting, aesthetic photonics, and wearable displays. Spatial control of anodization provides lithography-free patterning that is inherently scalable. Moreover, because anodization is compatible with large-area industrial practice, the method offers strong potential for translation from centimeter-scale demonstrations to wafer-level substrates and industrial components.

Conclusions

We demonstrated a meta-MIM device incorporating a nanoporous AAO layer enabling structural coloration independent of FP cavity thickness. By shifting from geometry-constrained to porosity-driven design, we establish index modulation as a new general lever in nanophotonics. This approach allows precise color tuning while maintaining a constant physical thickness and avoiding the need for multiple lithographic steps. The fabricated structures exhibited well-defined resonant transmittance peaks, with slight red-shifts compared to simulated values due to process-induced imperfections such as surface roughness and pore irregularity. Nevertheless, the measured spectral properties confirm the validity of the proposed design, and further optimization of pore ordering and film uniformity is expected to improve both color purity and optical efficiency. Our structure demonstrated spatially resolved multicolor rendering on a single substrate. Artistic and functional imagery—including a *Nadia aux cheveux lisses* by Henri Matisse and a university nameplate (KNU)—were successfully patterned. The ability to generate vivid, high-purity colors over large areas without lithography or thickness modulation highlights the versatility and scalability of the system. Because anodization is already used for large aluminum components, including aircraft wings, the method is inherently scalable to wafer-level and industrial dimensions. This compatibility highlights potential in displays, anti-counterfeiting, wearable devices, photovoltaics, and sensing technologies.

Author contributions

Hyo Jong Cho (conceptualization: lead; data curation: lead; formal analysis: lead; methodology: lead; project administration: supporting; resources: equal; Software: lead; validation: lead; visualization: lead; writing – original draft: lead; writing – review

& editing: equal) Yun Seon Do (conceptualization: equal; funding acquisition: lead; investigation: lead; methodology: supporting; project administration: lead; supervision: lead; validation: lead; writing – original draft: equal; writing – review & editing: lead) Jun Yong Kim, PhD (data curation: supporting; methodology: supporting; resources: supporting) Ki Won Jeong (data curation: supporting; methodology: supporting; resources: supporting) Soo-Hwan Jeong, PhD (conceptualization: supporting; methodology: equal; supervision: equal; validation: supporting; writing – review & editing: equal).

Conflicts of interest

There are no conflicts of interest to declare.

Data availability

All data supporting the findings of this study are available within the article and its supplementary information (SI). Supplementary information is available. See DOI: **https://doi.org/10.1039/d5mh01677k**.

Acknowledgements

This work was supported by the Alchemist Project grant funded by Korea Planning & Evaluation Institute of Industrial Technology (KEIT) & the Korean Government (MOTIE) (Project Numbers: 1415185027 and 20019169) and by the National Research Foundation of Korea (NRF) grant funded by the Korean government (MSIT) (RS-2024-00431341).

References

1 H. Zollinger, *Color Chemistry: Synthesis, Properties and Applications of Organic Dyes and Pigments*, Wiley-VCH, Weinheim, 2003.
2 P. Bamfield and G. Hutchings, *Chromic Phenomena: The Technological Applications of Colour Chemistry*, The Royal Society of Chemistry, Cambridge, 2001.
3 A. A. Gitelson, C. Buschmann and H. K. Lichtenthaler, *Remote Sens. Environ.*, 1999, **69**, 296.
4 I. Valyi-Nagy, K. J. Kaffka, J. M. Jako, E. Gonczol and G. Domjan, *Clin. Chim. Acta*, 1997, **264**, 117–125.
5 J. Wang, X. Guo, C. Li, H. Zhou, Y. Yan, F. Zhu, J. Wang, G. Cai and O. G. Schmidt, *Adv. Funct. Mater.*, 2025, **35**, 2416812.
6 H. J. Cho and Y. S. Do, *Opt. Mater.*, 2025, **162**, 116831.
7 J. Y. Kim, S. Y. Lee, K. H. Cho and Y. S. Do, *Adv. Funct. Mater.*, 2023, **33**, 2305528.
8 Y. Lim, B. Kang and S. Lee, *Adv. Funct. Mater.*, 2021, **31**, 2100839.
9 Y. Lim, B. Kang, S. J. Hong, H. Son, E. Im, J. Bang and S. Lee, *Adv. Funct. Mater.*, 2021, **31**, 2104105.
10 P. Pottier, M. J. Strain and M. Packirisamy, *ACS Photonics*, 2014, **1**, 430–436.
11 J. C. Blake, S. Rossi, M. P. Jonsson and A. Dahlin, *Adv. Opt. Mater.*, 2022, **10**, 2200471.
12 M.-S. Ahn, C. S. H. Hwang and K.-H. Jeong, *Adv. Opt. Mater.*, 2021, **9**, 2002036.
13 T. Xiao and P. Diao, *Adv. Mater.*, 2025, **37**, 2501069.
14 X. Cao, Y. Du, Y. Guo, G. Hu, M. Zhang, L. Wang, J. Zhou, Q. Gao, P. Fischer, J. Wang, S. Stavrakis and A. DeMello, *Adv. Mater.*, 2022, **34**, 2109161.
15 H. Gao, Y. Liang, Y. Huang, H. Huang and W. Peng, *Opt. Express*, 2022, **30**, 31136.
16 Z. Wang, S. Yi, A. Chen, M. Zhou, T. S. Luk, A. James, J. Nogan, W. Ross, G. Joe, A. Shahsafi, K. X. Wang, M. A. Kats and Z. Yu, *Nat. Commun.*, 2019, **10**, 1020.
17 J. Oakes, *Rev. Prog. Color. Relat. Top.*, 2001, **31**, 22–28.
18 E. Enríquez, J. J. Reinosa, V. Fuertes and J. F. Fernández, *Ceram. Int.*, 2022, **48**, 31080–31101.
19 K. T. P. Lim, H. Liu, Y. Liu and J. K. W. Yang, *Nat. Commun.*, 2019, **10**, 25.
20 Z. Dong, J. Ho, Y. F. Yu, Y. H. Fu, R. Paniagua-Dominguez, S. Wang, A. I. Kuznetsov and J. K. W. Yang, *Nano Lett.*, 2017, **17**, 7620–7628.
21 B. Deng, Y. Li, Z. Lu, K. Zheng, T. Xu, S. Wang, X. Luo, B. Grandidier, J. Zhang and F. Zhu, *Nat. Commun.*, 2025, **16**, 597.
22 G. E. Thompson, R. C. Furneaux, G. C. Wood, J. A. Richardson and J. S. Goode, *Nature*, 1978, **272**, 433–435.
23 L. Chen, Z. Qin and S. Chen, *Small Methods*, 2022, **6**, 2101090.
24 M. J. Park, S. K. Kim, R. Pode and J. H. Kwon, *Org. Electron.*, 2018, **52**, 153–158.
25 J. Y. Lee, US Pat. Appl. Publ., 2005/0110398 A1, 2005.
26 S. K. Kim, M. J. Park, R. Lampande, S. W. Jung, H. Park, J. K. Jeong and J. H. Kwon, *Org. Electron.*, 2020, **87**, 105938.
27 M. Ghahremani, A. McClung, B. Mirzapourbeinekalaye, A. A. Moughames, A. Karimi, M. G. Wood, M. Khavasi, C. Williams, S. Larouche and A. Adibi, *Nat. Commun.*, 2024, **15**, 8864.
28 Z. Chen, Z. Man, S. Rao, H. Hu, W. Shi, C. Zhang, Y. Zhang, J. Zhang, J. Liang and B. Xu, *Light: Sci. Appl.*, 2025, **14**, 251.
29 Z. Liu, H. Cao, X. Tang, H. Wu, T. Li, Y. Sun, J. Duan, K. Wang, J. Zhao, Z. Xiao, C. Xu, J. Wu, J. Kang and X. Xu, *Light: Sci. Appl.*, 2025, **14**, 64.
30 M. P. Martínez-Viademonte, S. T. Abrahami, T. Hack, M. Burchardt and H. Terryn, *Coatings*, 2020, **10**, 1106.
31 H. Masuda and K. Fukuda, *Science*, 1995, **268**, 1466–1468.
32 O. Jessensky, F. Müller and U. Gösele, *Appl. Phys. Lett.*, 1998, **72**, 1173–1175.
33 C.-A. Ku, C.-Y. Ku, M.-H. Kuo and Y.-C. Chang, *Nanomaterials*, 2023, **13**, 2853.
34 K. Nielsch, J. Choi, K. Schwirn, R. B. Wehrspohn and U. Gösele, *Nano Lett.*, 2002, **2**, 677–680.
35 B. Chen and K. Lu, *Langmuir*, 2011, **27**, 4117–4125.
36 C. Sun, J. Luo, L. Wu and J. Zhang, *ACS Appl. Mater. Interfaces*, 2010, **2**, 1299–1302.
37 A. Keshavarz, Z. Parang and A. Nasseri, *J. Nanostruct. Chem.*, 2013, **3**, 34.
38 Y. Ma, Y. Wen, J. Li, Y. Li, Z. Zhang, C. Feng and R. Sun, *Sci. Rep.*, 2016, **6**, 39165.
39 J. Kim, H. Kim, H. Kang, W. Kim, Y. Chen, J. Choi, H. Lee and J. Rho, *Nat. Food*, 2024, **5**, 293–300.

40 Z. Lu, K. Zheng, T. Xu, S. Wang, X. Luo, B. Grandidier, J. Zhang and F. Zhu, *Nat. Photonics*, 2018, **12**, 343–348.
41 B. Ko, J. Kim, Y. Yang, T. Badloe, J. Park, M. Jeong, H. Kang and J. Rho, *Adv. Sci.*, 2023, **10**, 2204469.
42 B. Ko, J. Kim, Y. Yang, T. Badloe, J. Park, M. Jeong, H. Kang, C. Jung, Y. Song and J. Rho, *Adv. Sci.*, 2025, **12**, 2409371.
43 Z. Lu, K. Zheng, T. Xu, S. Wang, X. Luo, B. Grandidier, J. Zhang and F. Zhu, *Nat. Commun.*, 2019, **10**, 4340.
44 B. Ko, T. Badloe, Y. Yang, J. Park, J. Kim, H. Jeong, C. Jung and J. Rho, *Nat. Commun.*, 2022, **13**, 6256.
45 K. Li, T. Li, T. Zhang, H. Li, A. Li, Z. Li, X. Lai, X. Hou, Y. Wang, L. Shi, M. Li and Y. Song, *Sci. Adv.*, 2021, **7**, eabh1992.
46 J. Proust, F. Bedu, B. Gallas, I. Ozerov and N. Bonod, *ACS Nano*, 2016, **10**, 7761–7767.
47 V. Vashistha, G. Vaidya, P. Gruszecki, A. E. Serebryannikov and M. Krawczyk, *Sci. Rep.*, 2017, **7**, 8092.
48 R. C. Devlin, M. Khorasaninejad, W. T. Chen, J. Oh and F. Capasso, *Proc. Natl. Acad. Sci. U. S. A.*, 2016, **113**, 10473–10478.
49 E. Heydari, J. R. Sperling, S. L. Neale and A. W. Clark, *Adv. Funct. Mater.*, 2017, **27**, 1701866.
50 T. Xu, H. Shi, Y.-K. Wu, A. F. Kaplan, J. G. Ok and L. J. Guo, *Small*, 2011, **7**, 3128–3136.
51 T. Xu, Y.-K. Wu, X. Luo and L. J. Guo, *Nat. Commun.*, 2010, **1**, 59.